International Journal of Pharmaceutics xxx (xxxx) 122869

Contents lists available at ScienceDirect

International Journal of Pharmaceutics

journal homepage: www.elsevier.com/locate/ijpharm

Characterization of the hydrochloride salt hemihydrate as a new salt of the antifungal agent tioconazole

Aldana B. Moroni[a], Elena Pérez Mayoral[b], Diego F. Lionello[c], Daniel R. Vega[d], Teodoro S. Kaufman[a,*], Natalia L. Calvo[a,*]

[a] *Área de Análisis de Medicamentos, Facultad de Ciencias Bioquímicas y Farmacéuticas, Universidad Nacional de Rosario e Instituto de Química Rosario (IQUIR CONICET-UNR), Suipacha 531, S2002LRK, Rosario, Argentina*

[b] *Departamento de Química Inorgánica y Química Técnica, Universidad Nacional de Educación a Distancia, UNED, Urbanización Monte Rozas, Avenida Esparta s/n, Ctra. de Las Rozas al Escorial Km 5, 28232 Las Rozas-Madrid, Spain*

[c] *Departamento Física de la Materia Condensada, Gerencia de Investigación y Aplicaciones, Centro Atómico Constituyentes, Comisión Nacional de Energía Atómica e Instituto Jorge A. Sabato, Universidad Nacional General San Martín, Av. Gral. Paz 1499, B1650KNA, San Martín, Buenos Aires, Argentina*

[d] *Departamento Física de la Materia Condensada, Gerencia de Investigación y Aplicaciones, Centro Atómico Constituyentes, Comisión Nacional de Energía Atómica y Escuela de Ciencia y Tecnología, Universidad Nacional General San Martín, Av. Gral. Paz 1499, B1650KNA, San Martín, Buenos Aires, Argentina*

ARTICLE INFO

Keywords:
Intrinsic dissolution
Salt formation
Solid-state characterization
Tioconazole hydrochloride hemihydrate
Thermal methods
Vibrational and NMR spectroscopies
X-ray diffractometry and crystal structure

ABSTRACT

Tioconazole is an effective antifungal agent, which has a very low solubility in aqueous media, that limits its bioavailability and efficacy. In an effort to overcome the drug limitations by improving its solubility, the hydrochloride salt was prepared in methanolic 1 M HCl and obtained as the hemihydrate, as demonstrated by elemental analysis. Single crystals were grown by slow evaporation from an aqueous 1 M HCl solution and their structure was determined using single-crystal X-ray diffraction at 302 K. The structures resulting from dehydration and further rehydration were also assessed, at 333 and 283 K, respectively. The morphology of the crystal, which exhibited birefringence under polarized light, was verified by hot stage microscopy. The solid was characterized by additional means, including thermal analysis (melting point, differential scanning calorimetry and thermogravimetry), spectroscopic methods (mid infrared, near infrared, ^{1}H, ^{13}C and ^{15}N nuclear magnetic resonance in solution, as well as ^{13}C and ^{15}N solid state with spinning at the magic angle) and X-ray diffraction techniques. Functional evaluation tests, including the intrinsic dissolution rate and the dissolution of powders were also performed. In the intrinsic dissolution rate test, the salt proved to dissolve over 2000 times faster than tioconazole. The results suggest that the new salt has physicochemical and performance properties which may support its use as a replacement of the free base in certain applications, especially where improved dissolution rate, solubility or bioavailability of the drug would be desired.

1. Introduction

Active pharmaceutical ingredients (APIs) can be prepared and used in various forms, the nature of which is of eminent importance in relation to industrial scale-up, ease of manipulation and even pharmacological activity. APIs are mainly marketed as solids, the latter being most frequently prepared in a crystalline form.

Most salts are crystalline materials, which contain in the same lattice two or more different components in an ionized state and subjected to ionic interactions. Pharmaceutical salt formation represents a unique opportunity to generate new compounds with improved properties; currently, it is the most preferred and effective method to enhance some critical physicochemical properties of the APIs, such as solubility, bioavailability, stability, dissolution rate and processability, including their ability to undergo tableting, among others. It has been estimated that half of all drug molecules used in medicinal therapy are administered as salts (Bharate, 2021).

Solid-state characterization is of paramount importance, because it provides key information related to the physicochemical and functional properties of the APIs. Currently, this is considered a multidimensional task, that encompasses numerous scientific disciplines within materials science (Vioglio et al., 2017), and that provides results with impact on numerous areas of the pharmaceutical science.

---

* Corresponding authors.
E-mail addresses: kaufman@iquir-conicet.gov.ar (T.S. Kaufman), calvo@iquir-conicet.gov.ar (N.L. Calvo).

https://doi.org/10.1016/j.ijpharm.2023.122869
Received 25 October 2022; Received in revised form 14 March 2023; Accepted 15 March 2023
0378-5173/© 20XX

Tioconazole (TCZ, Figure S1) is 1-(2-[(2-chloro-thien-3-yl) methoxy]-2-[2,4-dichloro phenyl]ethyl)-1*H*-imidazole; the compound is an imidazole antifungal agent with a broad spectrum of activity, being useful against dermatophytes and other fungi, including *Candida albicans* and *Malassezia furfur*. Its main use is for the treatment of recurrent vaginal candidiasis, but it is also employed topically for nail infections, and as a lotion, topical cream or in powder form, for the treatment of superficial fungal infections.

The commercial solid yields colorless monoclinic crystals, the structure of which has been elucidated by single crystal X-ray diffractometry (SC-XRD) (Kljun et al., 2014). The drug has one stereogenic center, and the separation of its enantiomers by capillary electrophoresis-mediated has been reported (Penn et al., 1994). TCZ is a white or almost white solid with a low melting point (80 °C) (Crisostomo-Lucas et al., 2015), being weakly basic (pK_a: 6.51–6.61) due to its imidazole ring (Sanli et al., 2013). The log POW (partition octanol:water) of the drug is 4.23–4.86 (Stratton et al., 2015; Brown et al., 2021), and its solubility in water (16.5 mg l^{-1}) is very low, being reduced to 1.7 mg l^{-1} at pH 6.8 (phosphate buffer) (Drozd et al., 2021), all of which limit its bioavailability and antifungal activity.

The solubility problem has long been an issue of concern, which has been addressed by different research groups (Yang et al., 2008). Among others, the formation of inclusion complexes (Van Doorne et al., 1988) with α-cyclodextrin, β-cyclodextrin (Penn et al., 1994; Kiss et al., 2019), and substituted cyclodextrins (Penn et al., 1993) and the design of special carriers (Pienko et al., 2017) have been reported as means to overcome this drawback, and improve the pharmacokinetics and efficacy of the antifungal agent. Similarly, drug delivery strategies have been explored to obtain solids with better wetting and dissolution properties of TCZ, aiming to enhance their bioavailability and enhance the therapeutic efficacy (Yang et al., 2008). These include emulgels (Sah et al., 2017), nanocapsule suspensions (Flores et al., 2017b), lipid nanoparticles (Flores et al., 2017a), and spray-dried powders (Ribeiro et al., 2016). In addition, the group of Perlovich has recently reported the characterization of dicarboxylic acid salts of TCZ (oxalic, malonic, fumaric, DL-tartaric) as more soluble alternatives to TCZ (Drozd et al., 2021).

On the other hand, formation of the hydrochloride has been used as a TCZ purification strategy (Gymer, 1977), whereas use of the “hydrochloride salt” of TCZ for pharmaceutical purposes has been included in a patent (Koral et al., 1999). However, in neither case the preparation and physicochemical properties of the salt were disclosed.

As part of our interest in studying the properties of TCZ, we have performed an exhaustive characterization of the drug (Calvo et al., 2019a) and developed new alternatives for its delivery, based on chitosan nanoformulations (Calvo et al., 2019b) and chitosan-hydroxypropyl methylcellulose films (Calvo et al., 2019c). In pursuit of our interest in this API, herein we report the characterization of tioconazole hydrochloride hemihydrate (TCZHCl•½H_2O) as a new salt of the API.

2. Materials and methods

2.1. API and chemicals

Pharmaceutical grade TCZ bulk drug was kindly donated by Panalab Laboratories (Buenos Aires, Argentina). Double distilled water was used. All solvents employed were of analytical grade.

2.2. Preparation of TCZ hydrochloride hemihydrate (TCZHCl•½H_2O)

TCZ (400 mg) was dissolved in methanolic 1 M HCl (25.8 ml, molar ratio TCZ:HCl = 1:25), and the resulting solution was concentrated at 40 °C under reduced pressure, using a rotary evaporator (Büchi, Switzerland). For the SC-XRD experiments, a supersaturated solution of TCZ in 1 M HCl was left to stand at room temperature until formation of crystals. Each lot was kept in a desiccator and protected from light during the study.

2.3. Hot stage microscopy

Thermal microscopy analysis was carried out using an Leitz model 350 optical microscope (Ernst Leitz, GmbH, Wetzlar, Germany), fitted with a controllable heating plate and a 4 × Beion CMOS USB-digital camera (Shanghai Beion Medical Technology Co., Ltd., Shanghai, China) of 5.0 megapixels [resolution 2592 × 1944 (H × V)]. A crystalline sample was placed between two laboratory glasses into the heating plate cell, which was set under the objective lens of the microscope. The plate was heated at different rates until the melting point was reached. Changes in crystal morphology and phase transitions in the sample were detected visually and using the USB-camera.

2.4. Elemental analysis

Elemental analyses were carried out with a LECO CHNS-932 elemental analyzer (LECO Corp., Benton Harbor, USA).

2.5. Thermal methods

2.5.1. Differential scanning calorimetry

Differential scanning calorimetry (DSC) curves were acquired with a Linseis PT1000 thermal analyzer (Linseis Messgeraete GmbH, Selb, Germany), operating under constant nitrogen flow (130 ml min^{-1}). The samples (~5 mg) were placed in open aluminum pans and heated at a rate of 10 °C min^{-1} between 40 and 230 °C. An empty pan was used as reference.

2.5.2. Thermogravimetric analysis

Thermogravimetric analysis (TGA) measurements were carried out on a TA Instruments Q600 apparatus (TA Instruments, New Castle, USA). The samples (~8 mg) were placed in alumina crucibles and heated at a rate of 10 °C min^{-1} from room temperature to 600 °C under nitrogen (flow rate = 100 ml min^{-1}), as the purge gas.

2.6. Vibrational spectroscopy studies

2.6.1. Mid-infrared spectroscopy

Mid-infrared (MIR) spectra were acquired in a Shimadzu Prestige 21 FTIR instrument (Shimadzu Corp., Kyoto, Japan), using a diamond-based ATR accessory GladiATR (Pike Technologies, Madison, USA), fitted with a Pike temperature control unit. A fixed number of 20 scans per sample (~20 mg) was performed, at a resolution of 4 cm^{-1}, over a wavenumber range of 4000–400 cm^{-1}.

2.6.2. Near infrared spectroscopy

Near infrared (NIR) spectra were obtained at room temperature with a NIRS DS2500 spectrometer (FOSS, Hillerød, Denmark) in reflectance mode, with the samples (~500 mg) placed in a circular quartz cell for solids. The spectral data were collected in the spectral range 700–2500 nm, as an average of 7 scans/spectrum, at a resolution of 0.5 nm.

2.7. Nuclear magnetic resonance (NMR) spectroscopy

2.7.1. Solution NMR

Solution NMR spectra were recorded on a Bruker spectrometer (400.13 MHz for ^1H, 100.62 MHz for ^{13}C and 40.54 MHz for ^{15}N) at 300 K, equipped with a 5-mm inverse detection H-X probe and a z-gradient coil (Bruker Biospin, Rheinstetten, Germany). All NMR spectra were acquired and analyzed using Bruker’s Topspin v.4.0.6 software.

The chemical shifts are informed in ppm, in the δ scale, and were obtained with regards to the residual peaks of the solvent (DMSO-d_6: δ = 2.49 ppm for ^{1}H and δ = 39.5 ppm for ^{13}C). The WALTZ-16 sequence was used for broadband proton decoupling during the ^{13}C experiments. Nitromethane was used as external reference for the ^{15}N experiments. The spectra were acquired using a 2D (^{1}H-^{15}N) gradient selected Heteronuclear Multiple Bond Correlation (HMBC) by means of standard pulse sequences and in the absolute mode.

2.7.2. Solid state NMR

Solid state ^{13}C (100.73 MHz) and ^{15}N (40.60 MHz) NMR spectra were obtained on a Bruker WB 400 spectrometer (Bruker Biospin, Rheinstetten, Germany) at 300 K using a 4-mm DVT probehead and the CP-MAS technique. Samples were carefully packed in a 4-mm diameter cylindrical zirconia rotor with Kel-F end-caps. The ^{13}C spectra were originally referenced to a glycine sample and then the chemical shifts were recalculated to the Me_4Si [for $C = O$ of glycine, δ = 176.1 ppm)] and ^{15}N spectra to $^{15}NH_4Cl$ and then converted to the nitromethane scale using the relationship: $\delta\ ^{15}N_{MeNO2} = \delta\ ^{15}N_{NH4Cl} - 338.1$ ppm. Typical acquisition parameters for the ^{13}C CPMAS experiments were: 90° ^{1}H pulse: 3.2 μs, ^{1}H decoupling sequence: SPINAL 64 (Fung et al., 2000) and spectral width: 40 kHz; recycle delay: 120 s; acquisition time: 30 ms; contact time: 4 ms and spin rate: 12 kHz. Typical acquisition parameters for ^{15}N CPMAS were: ^{1}H 90° pulse: 3.2 μs; ^{1}H decoupling sequence: SPINAL 64 and spectral width: 40 kHz; recycle delay: 120 s; acquisition time: 35 ms; contact time: 9 ms and spin rate: 6 kHz. The protonated nitrogen atom (N–H subspectum) was detected by recording the CP-MAS spectrum with a contact time of 0.5 ms.

2.8. X-ray diffraction experiments

2.8.1. Powder X-ray diffraction

Powder X-ray diffraction (PXRD) patterns were acquired in a PANalytical X'Pert PRO diffractometer (Malvern Panalytical Ltd., Malvern, UK), operated at 45 kV and a current of 40 mA. Samples were placed in a zero-background sample holder at room temperature, which was rotated. Data were obtained over the 2θ range of 5-50°, at a step size of 0.04° and a counting time of 20 s, employing Cu Kα radiation (1.54184 Å) and a soller slit of 0.04 rad.

2.8.2. Single crystal X-ray diffraction

SC-XRD data were collected on a 0.400 × 0.300 × 0.200 mm^3 crystal using a Bruker D8 QUEST ECO diffractometer (Bruker AXS GmbH, Karlsruhe, Germany), with MoK radiation (λ = 0.71073 Å) at different temperatures, attained with an open-flow nitrogen gas Oxford Cryosystems cooler (Oxford Cryosystems Ltd., Long Hanborough, UK). The data collection strategy and data reduction followed standard procedures implemented in the APEX3 software from Bruker. The structures were solved using SHELXS-97 (Sheldrick, 2008) and refined using the full-matrix least-squares procedure with SHELXL2018/1 (Sheldrick, 2015). All H atoms were initially found in a difference map; those attached to C were further idealized [C–H (sp^2): 0.93 Å; C—H2 (sp^3): 0.97 Å] and refined using a riding model, while those attached to X = N were refined with restrained distances [N–H = 0.86 (1) Å]. In all cases, isotropic U_{iso}(H) = 1.2Ueq (X) were used. Multi-scan absorption correction was performed using SADABS 2016/2 (Krause et al., 2015). WinGX (Farrugia, 2012) and PLATON (Spek, 2009) were used to prepare material for publication. The crystal structure data (Tables S4-S10) were deposited in the form of cif files with the Cambridge Crystallographic Data Centre (CCDC). This information can be obtained free of charge upon request from CCDC via https://www.ccdc.cam.ac.uk/data_request/cif.

2.9. Determination of the intrinsic dissolution rate

The test was performed employing the stationary disk method and a Hanson SR8-Plus dissolution station (Hanson Research, Chatsworth, USA), configured as USP apparatus II (paddles). The dissolution medium was double distilled water (500 ml) at 37 ± 0.5 °C and the paddle rotation rate was 50 rpm. The disks were prepared by compression of the test powder (135 mg) in a Perkin Elmer (Perkin Elmer, Norwalk, USA) hydraulic press (20 min at 4 Ton $inch^{-2}$) to obtain disks (I.D. = 13 mm; surface area = 1.33 cm^2) that would not disintegrate during the test.

The disks were inserted into a stainless steel holder, so that only one face was exposed to the dissolution medium. Samples (3 ml) were taken at pre-specified times, without replenishment and filtered, discarding the first drops, and suitable aliquots were properly diluted with H_2O. A nine point calibration curve (range = 1.9–25 μg ml^{-1}) was concomitantly prepared by dilution of a stock standard solution of TCZ (151 μg ml^{-1}) in acetonitrile. The assay for drug content was performed with a 8453 UV–DAD UV–Vis spectrophotometer (Agilent Technologies, Santa Clara, USA) fitted with a quartz cell of 10 mm optical path length, employing absorbance measurements at 225 nm (Calvo et al., 2019c). Triplicate determinations were performed. The intrinsic dissolution rate (IDR) was calculated from the slope of the straight line of the cumulative drug release graph, obtained by linear regression of the first five points.

2.10. Powder dissolution rate

The experiments were performed with samples containing an equivalent to 65 mg tioconazole, in a Hanson SR8-Plus dissolution station (Hanson Research, Chatsworth, USA), configured as USP apparatus II (paddles), using acetate buffer (0.266 M, pH 4.5) and double distilled water as dissolution media (500 ml), kept at 37 ± 0.5 °C. The paddle rotation rate was 50 rpm. The powders were directly poured into the medium. Aliquots (2 ml) of the dissolution medium were withdrawn at pre-established times and processed as indicated under *Determination of the intrinsic dissolution rate*. The dissolution experiments were continued up to 24 h (1440 min).

2.11. Data analysis and graphics software

Graphs and statistical data analysis were performed using Origin 8.5 (OriginLab Co., Northampton, USA).

3. Results and discussion

3.1. Preparation of the solid state forms

The pKa difference between TCZ (pK_a = 6.51–6.61) and HCl (pK_a = -6) exceeds 4 units. According to the p*K*a rule, which states that when $\Delta pK_a < 1$ mostly cocrystals are formed, whereas salts are produced exclusively when $\Delta pK_a > 4$ (Hossain Mithu et al., 2021), salt formation should be expected in this case.

The new solid was prepared by reduced pressure concentration of a methanolic HCl solution of TCZ at room temperature. This phase was obtained as colorless plates, which exhibited birefringence when illuminated with polarized light (Fig. 1). No changes were observed in the solid upon heating until its melting point, except for a slight opacification, in agreement with its loss of water.

3.2. Characterization of the new solid

3.2.1. Elemental analysis

The elemental constitution of both, TCZ and the new solid phase, was analyzed in order to ascertain their chemical composition. As ex-

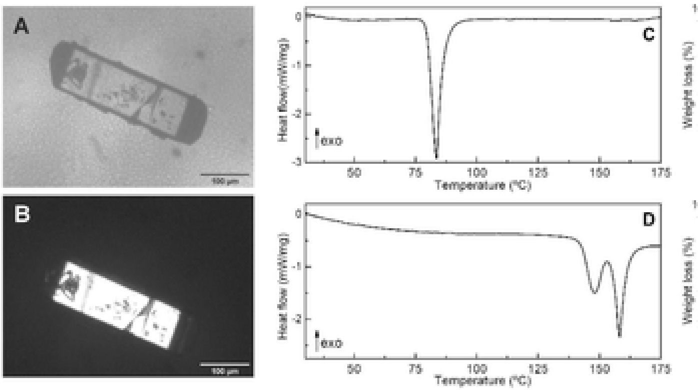

Fig. 1. Left: Optical microscopy image of a TCZHCl•½H_2O crystal at room temperature. Under non-polarized light (A) and under polarized light (B). Right: Thermal behavior of TCZ and TCZHCl•½H_2O. DSC profiles of TCZ (C) and TCZHCl•½H_2O (D), along with the corresponding TGA and DTGA curves of TCZ (E) and TCZHCl•½H_2O (F).

pected, in the case of TCZ, the results complied with those expected for its formula, whereas those of the salt were in good agreement with the composition of a hydrochloride hemihydrate salt (Table S1).

3.2.2. Thermal analysis

DSC is useful to record the thermal transitions as well as the corresponding latent heats of the solids under study, whereas TGA is an essential technique to determine the thermal stability of the analytes, by monitoring their weight loss in an inert atmosphere as a function of temperature.

The DSC curve of TCZ (Fig. 1C) displayed a single endothermic peak at 83.5 °C, with T_{onset} about 79.1 °C and a latent heat of about −82 J g^{-1} (Calvo et al., 2019a). As evidenced from optical microscopy, this event is related to the melting point of the pure crystalline drug and does not involve weight loss, as observed in the TGA curve (Fig. 1E), confirming that it is an anhydrous form. The latter also revealed that TCZ is stable up to 165 °C, when decomposition is initiated. At 241 °C, barely a 5% decomposition level is observed, whereas 98.75% mass loss was recorded at 325 °C (Blokhina et al., 2021).

As for TCZHCl•½H_2O, its DSC profile (Fig. 1D) showed three easily distinguishable events. The first one was endothermic, took place from room temperature up to 90 °C and was associated with a weight loss of 2.10%, which yielded an anhydrate, as observed in the corresponding TGA curve (Fig. 1F). This loss is fully consistent with the theoretical value expected for the escape of H_2O from the lattice of a hydrochloride hemihydrate phase (~2.08%). Half of the water loss occurred below 90 °C, suggesting that H_2O should be rather weakly bonded to TCZHCl. The relative ease of rehydration, detected by TGA (Figure S2) and in the SC-XRD experiments, also point to the same conclusion.

The new solid also experienced two additional endothermic events, with peaks centered at 147.8 °C (T_{onset} = 139.4 °C) and 158.2 °C, and corresponding latent heats of about −44.2 and −53.7 J g^{-1}, respectively. These events took place without loss of mass, as evidenced from the TGA results, suggesting the existence of a phase transformation process at the first peak to yield the final solid form, which undergoes melting at 158.2 °C (Gymer, 1977), without decomposition. This is reminiscing of the behavior found in the methanolic solvate of miconazole, a related antifungal agent (Panini et al., 2022).

Beginning at 175 °C, the salt experienced a mass loss that was attributed to the decomposition of the anhydrous hydrochloride; the loss reached 5% at 244 °C, while at 325 °C the process was almost complete, as stemmed from the recorded weight loss of 97.7%. Comparison between the thermally induced weight loss curves of TCZ and the salt (Fig. 1E and 1F) evidenced essentially similar thermal stability profiles for both solids.

3.2.3. Mid infrared spectroscopy

Analysis of the MIR spectra is appropriate to unveil structural changes related to the formation of the hydrate of the salt; diagnostic signals are useful evidence to identify TCZHCl•½H_2O and to differentiate the salt from TCZ. The spectrum of TCZHCl•½H_2O (Fig. 2A) displayed a rather broad O–H stretching band with a peak at 3493 cm^{-1}, which is absent in the spectrum of TCZ (Fig. 2B). This is in agreement with the expectations for a hydrated solid with an inter-molecularly hydrogen bonded system (Subashchandrabose et al., 2021). The shape and location of the band suggested that water in the solid is hydrogen bonded. Additionally, the salt exhibited wide and intense bands in the range 2700–2500 cm^{-1}, which are missing in the spectrum of TCZ.

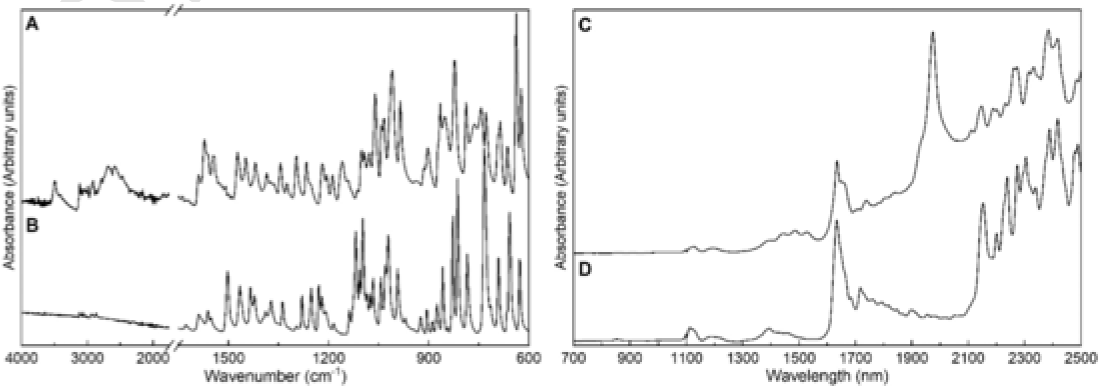

Fig. 2. Left: Stacked ATR/FT-IR spectra of TCZHCl•½H_2O (A) and TCZ (B), in the range 4000–600 cm^{-1}. Right: Stacked NIR spectra of TCZHCl•½H_2O (C) and TCZ (D), in the range 700–2500 nm.

These are probably due to the N–H stretching of the protonated nitrogen (Joshi et al., 2014).

Notably, the salt showed relatively more intense aromatic C–H and C = C stretching bands in the 3030 and 1630–1550 cm^{-1} regions than TCZ. Another spectral difference between the solids was found at the band corresponding to the C = N stretching of the imidazole group. In TCZ, this absorption was found at 1503 cm^{-1} but in the salt the band appeared at a higher wavenumber (1545 cm^{-1}).

Probably these shifts are related to conformational changes and modifications in the aromatic character of the imidazole ring as a consequence of protonation of the nitrogen atom. Finally, marked differences were observed in the whole fingerprint region (1500–600 cm^{-1}), supporting the formation of a new chemical entity. The list of relevant signals and their assignment is detailed in Table S2.

3.2.4. NIR spectroscopy

The NIR spectra of TCZHCl•½H_2O (Fig. 2C) and TCZ (Fig. 2D) in the 700–2500 nm region also proved to be different, the latter being consistent with the literature.[21] Obvious differences were observed in terms of the intensity and position of the bands in the region between 2200 and 2500 nm, which typically corresponds to CH and CH_2 combination bands. The same phenomenon occurred with the peaks located in the 2150–2200 nm region, that are associated with the combination bands of the N–H bonds, which could be due to the protonation of one of the N as a result of formation of the hydrochloride salt.

Interestingly, the spectrum of TCZHCl•½H_2O also displayed a high intensity peak at 1974 nm, along with others at 1192 and 1444 nm, which could be assigned to the presence of water. These signals at 1444 and 1974 nm can be attributed to the first overtone of the O–H stretching vibrations and combination of O–H stretching and bending vibrations, respectively (Chavan et al., 2017).

In the 1700–1800 nm wavelength interval, frequently associated with the first overtone of the CH and CH_2 stretching vibrations, TCZ shows a complex pattern of bands; however, TCZHCl•½H_2O displayed only a single peak at 1738 nm.

A more subtle difference was found in the band corresponding to the first overtone of the ArC–H stretching vibrations. TCZ presents a band centered at 1634 nm, whereas in the case of TCZHCl•½H_2O, the same absorption is shifted to 1635 nm and appears with lower intensity and with a marked shoulder. Probably, this band reflects changes resulting from protonation of one of the imidazole nitrogen atoms due to salt formation.

More differences in band positions were found between 1350 and 1550 nm, a region generally related to the first overtone of CH and CH_2 stretching vibrations and their combination bands, where the salt displays a pattern of four evenly spaced and strongly overlapped peaks (1399, 1444, 1486 and 1527 nm). Finally, the band located at 1112 nm in TCZ, which is shifted to 1127 nm in the spectrum of the salt can be assigned to the second overtone of the ArC–H stretching vibrations.

3.2.5. Solution ^1H and ^{13}C NMR spectra

NMR spectroscopy is a powerful tool for identification of organic compounds, being also sensitive to conformational and acid-base mediated changes in solution. The ^1H NMR spectrum provides information about the various kinds of protons according to their different magnetic environments as well as their orientation.

Fig. 3 displays the ^1H and ^{13}C NMR solution spectra of TCZ and TCZHCl•½H_2O. The complete and unambiguous assignment of all both spectra of the salt, which was performed with the assistance of standard 2D NMR techniques, including COSY, HSQC and HMBC spectra (Figures S3-S5), is shown in Table S3.

A close inspection of the spectra revealed many differences and that the most important changes resulting from salt formation took place in the atoms associated with the imidazole ring. For instance, in the ^1H NMR spectrum, the resonances of H1-H3 experienced different degrees of downfield shifts; H1 moved from $\delta = 7.45$ ppm in TCZ to $\delta = 9.04$ ppm, whereas H2 changed from $\delta = 6.84$ ppm to $\delta = 7.66$ ppm and the signal of H3 switched from $\delta = 7.01$ ppm to $\delta = 7.61$ ppm. The highest chemical shift variations, observed on H1 and H2, suggested that protonation took place at N_b, their closest nitrogen atom, as anticipated by an analysis of the acid-base properties of both nitrogen atoms of the heterocycle.

The proton-decoupled ^{13}C NMR spectrum of TCZHCl•½H_2O (Fig. 3C) displayed the expected 16 signals, as detailed in Table S3. A visual comparison with the spectrum of TCZ (Fig. 3D) revealed clear resonance changes for C1-C5 (the imidazole ring and the associated aliphatic chain), involving upfield and downfield chemical shift displacements. The magnitude of the chemical shift difference ($\Delta\delta_{C2} = 8.5$ ppm) further confirmed that protonation took place at the neighboring nitrogen atom (N_b).

On the other hand, variations among the chemical shifts of the side chain carbon atoms, which were also observed in the ^1H spectra, also suggested that protonation of N_b induced conformational changes in the imidazole ring and its side chain attached to N_a, with regards to TCZ.

3.2.6. Solid state NMR

3.2.6.1. *^{13}C ssNMR.* Solid-state NMR spectroscopy is a powerful non-destructive technique, useful for acquiring structural information on solid pharmaceutical systems. The ^{13}C solid-state NMR spectra of TCZ and TCZHCl•½H_2O are shown in Fig. 4A-4D.

Despite the resonances of the aliphatic carbon atoms are observed as rather narrow signals, both spectra contain less resonances than those expected in the aromatic region, which are observed as wide peaks with multiple and overlapped signals; this suggests that the crystal structures

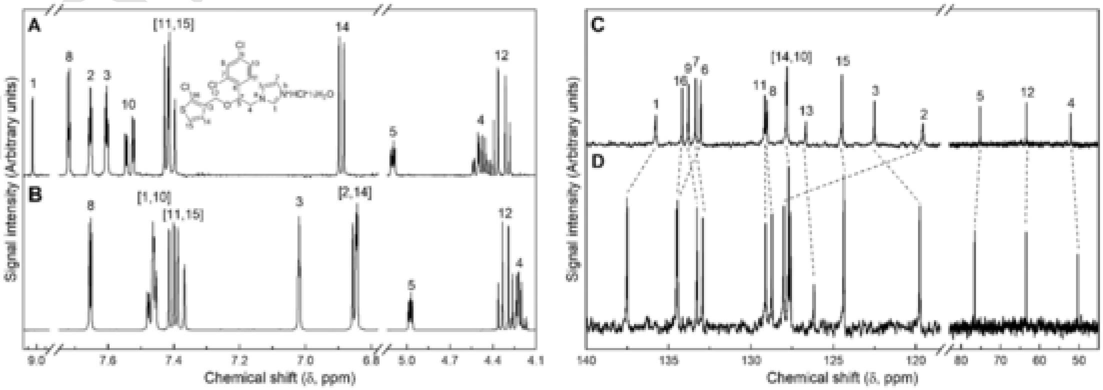

Fig. 3. Left: Stacked ^1H NMR spectra in DMSO-d_6 at 300 K of TCZHCl•½H_2O (A) and TCZ (B). Right: Stacked ^{13}C NMR spectra of TCZHCl•½H_2O (C) and TCZ (D) in DMSO-d_6 at 300 K. Proton and carbon atom numbers and dashed lines were added as visual aids.

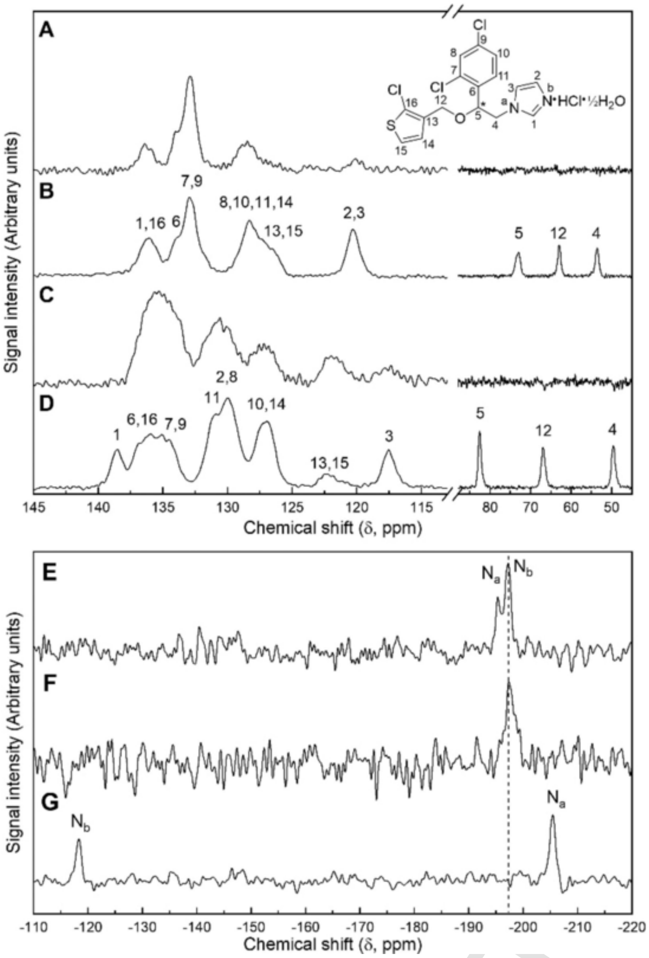

Fig. 4. Top: Stacked CP-MAS ^{13}C ssNMR spectra of TCZHCl•½H$_2$O (A and B) and TCZ (C and D). Sub-spectra (A) and (C) were acquired with the NQS pulse sequence. Bottom: Stacked CP-MAS ^{15}N ssNMR spectra of TCZHCl•½H$_2$O (E) and TCZ (G), and N–H subspectrum of TCZHCl•½H$_2$O (F).

are complex, and may carry more than one molecule in the corresponding crystallographic asymmetric units.

Tentative signal assignments were made (Fig. 4) by comparison with the ^{13}C NMR data of the compounds dissolved in DMSO-d_6 (Fig. 3C-3D and Table S3) and with the guide of the corresponding NQS (Non-Quaternary Supression) sub-spectra (Fig. 4A and 4C), which display only the quaternary carbon atom resonances.

3.2.6.2. ^{15}N ssNMR spectra. The ^{15}N ssNMR spectra are useful to identify the nitrogen atoms of the studied species according to their magnetic environment and to ascertain the site of protonation in the case of a salt. The spectra of both solids revealed a pair of resonances each, corresponding to the nitrogen atoms of the imidazole moiety (N$_a$ and N$_b$). In the case of TCZ (Fig. 4G), the peaks were observed at δ = -205.4 and −118.3 ppm and attributed to N$_a$ and N$_b$, respectively, by comparison with the ^{15}N HMBC solution spectrum taken in DMSO-d_6 (Figure S6), where these nitrogen atoms exhibited the corresponding resonances at δ = -212.0 (cross-peaks with H1, H2, H3 and H5) and −118.7 ppm (cross-peaks with H1, H2 and H3).

On the other hand, the signals in the spectrum of TCZHCl•½H$_2$O (Fig. 4E) were detected at δ = -196.1 and −194.1 ppm. The small difference between the resonances turned necessary the acquisition of a specific N–H subspectrum (Fig. 4F), to aid the unequivocal identification of N$_a$. In this way, the most shielded signal was unequivocally assigned to N$_b$.

Interestingly, in the solution ^{15}N HMBC spectrum (Figures S7 and S8), the signal of N$_a$ was found at δ = -203.3 ppm, as stemmed from its correlation with H1, H2, H3, H4 and H5, whereas the resonance of N$_b$ was observed at δ = -199.5 ppm, displaying cross-peaks with H1 and H2, meaning that the order of the signals was reversed with regards to the solid-state spectrum. This confirms that care should be taken when attempting to assign closely found ssNMR resonances by comparison with their solution counterparts, if the signals are too close.

The marked shielding experienced by N$_b$ (Δδ = -77.8 and −80.8 ppm for the solid and solution, respectively), combined with the slight deprotection suffered by N$_a$ (Δδ = +11.3 and + 8.7 ppm for the solid and solution, respectively), confirmed that N$_b$ supports protonation, and suggest that the positive charge is delocalized across the imidazole ring.

3.2.7. Powder X-ray diffraction

The powder X-ray diffractograms of TCZ and TCZHCl•½H$_2$O are represented in Fig. 5. The PXRD pattern of the drug employed for the preparation of the new phase (Fig. 5A) was congruent with the literature data for TCZ.[21] However, a comparison of the latter with that of the new solid phase (Fig. 5B) revealed a pattern of new reflections, with unique 2θ values that do not exist in the diffractogram of TCZ. This confirmed that the API had crystallized yielding a different structure.

The powder diffraction pattern of the new salt was also compared with that calculated from the structure refined by SC-XRD (Fig. 5C); the high correlation observed between them confirmed their identity and suggested lack of contamination with other TCZ solid forms. It can be assumed that minor differences between the relative intensities of the experimental and calculated diffraction patterns could be due to preferred orientation effects (Bunaciu et al., 2015). Ultimately, a number of peaks proved to be exclusive to crystalline TCZHCl•½H$_2$O, so they can be useful to identify the salt as such or as a contaminant in TCZ bulk drug.

3.2.8. Single-crystal X-ray diffraction

A suitable single crystal was selected and used as material for the analysis at three different temperatures (302 K, 333 K, and 283 K after the heating stage). Crystallographic data, data collection, and structure refinement details for TCZHCl•½H$_2$O at 283 K, 302 K, and 333 K are summarized in Table S4. All crystal structures were resolved and refined into the triclinic space group $P\overline{1}$, and Fig. 6 shows the corresponding molecular diagram (at 283 and 302 K) with the corresponding atom labeling. The atomic coordinates, torsion angles, bond lengths, and bond angles are provided as Supplementary Material (Tables S4-S10).

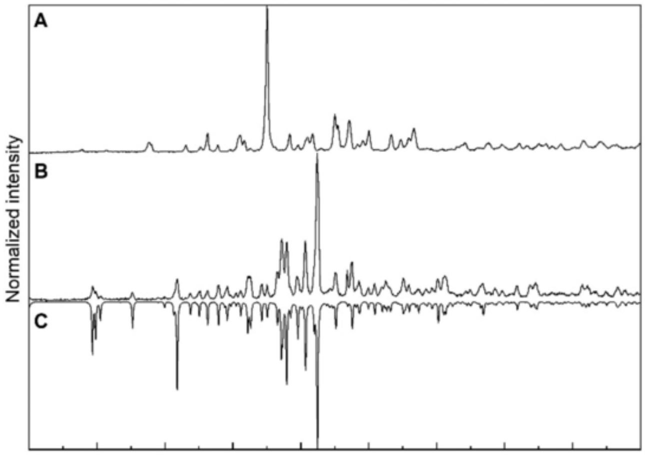

Fig. 5. Stacked PXRD diffractograms of (A) TCZ and (B) TCZHCl•½H$_2$O. Comparison with the theoretical diffractogram of TCZHCl•½H$_2$O (C).

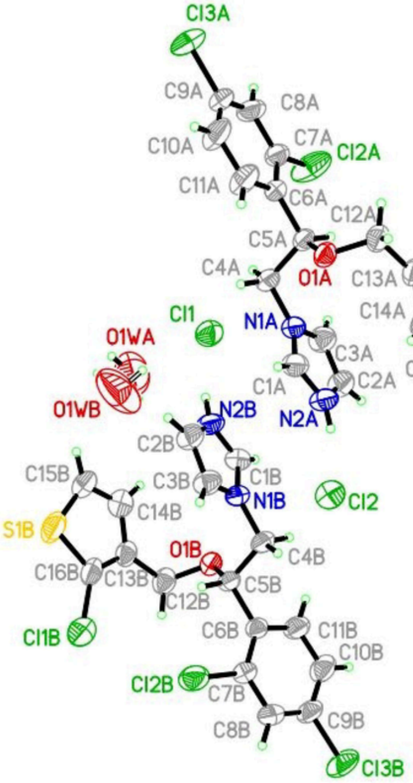

Fig. 6. ORTEP representation of TCZHCl•½H_2O at 302 K and 283 K showing the numbering scheme used and displacement ellipsoids drawn at the 50% probability level.

The structure at 302 K corresponds to a salt hemihydrate containing in the asymmetric unit two crystallographically independent $(TCZ)^+$ $(Cl)^-$ ionic pairs and one water molecule, with the following lattice parameters: a = 10.3995(5) Å, b = 11.0516(6) Å, c = 18.6950(9) Å, α = 78.245(2)°; β = 84.851(2)°, and γ = 84.851(2)°.

This phase is a channel hydrate, where the included water molecules of adjoining unit cells lie next to each other along the direction [1, −1, 0] of the lattice, forming a sort of “channels” through the crystal (Fig. 7). Noteworthy, each water molecule is disordered, displaying two positions with different occupancy factors (0.68 and 0.32). The internal C1-N2-C2 angle of the imidazole ring is 109.2(3)° for both molecules, which is within the range observed for similar imidazole salts, indicating the protonation of the N atom and the formation of a salt (Budagumpi et al., 2012; Drozd et al., 2021).

Compared to TCZ, and in agreement with previous inferences, it was also observed that the aromatic rings experienced conformational changes, tending to be more coplanar to each other. On the other hand, the solid undergoes partial dehydration upon heating. At 333 K, the asymmetric unit contains a single $(TCZ)^+$ $(Cl)^-$ ionic pair and only 10% of the original water molecules remain, resulting in a unit cell with smaller cell dimensions (V = 941 Å^3).

However, the solid retains the three-dimensional crystal structure of the hemihydrate, so both are isostructural. In each ionic pair, the counterions are associated by $N^+–H\cdots Cl^-$ interactions (Table S6). When the previously heated solid was cooled down to 283 K recovery of both, the volume of the orginal unit cell and the percentage of water, were observed; this behavior, which is to be expected for a channel hydrate, was confirmed by TGA (Figure S2).

3.2.9. Dissolution of the solids

3.2.9.1. Intrinsic dissolution rate. IDR refers to the amount of drug dissolved per unit time per unit area of a pure drug substance under conditions of constant surface area, composition of the dissolution medium and rotation speed. Being related to the rate of mass transfer from a solid surface to the liquid phase, it is a kinetic parameter that is useful to characterize solid drugs (Etherson et al., 2020; Zakeri-Milani et al., 2009). IDR is a rate phenomenon; therefore, it might be expected to correlate more closely than solubility with in vivo drug dissolution dynamics.

A comparison between the dissolved masses of TCZ and TCZHCl•½H_2O is shown in Fig. 8, revealing that the salt is much more soluble than the parent drug. In addition, the dissolution rates were rather constant during the initial part of the experiments, enabling execution of linear regressions with good correlation coefficients.

The results indicate that the dissolution rate constants are significantly different. Kaplan suggested that drugs with an aqueous IDR of $<1.8 \times 10^{-3}$ mg cm^{-2} s^{-1} are highly likely to exhibit dissolution rate-limited absorption (Kaplan, 1972); this is the case of TCZ, which displayed an IDR value of 8.77×10^{-5} mg cm^{-2} s^{-1} (r^2 = 0.9993, n = 5).

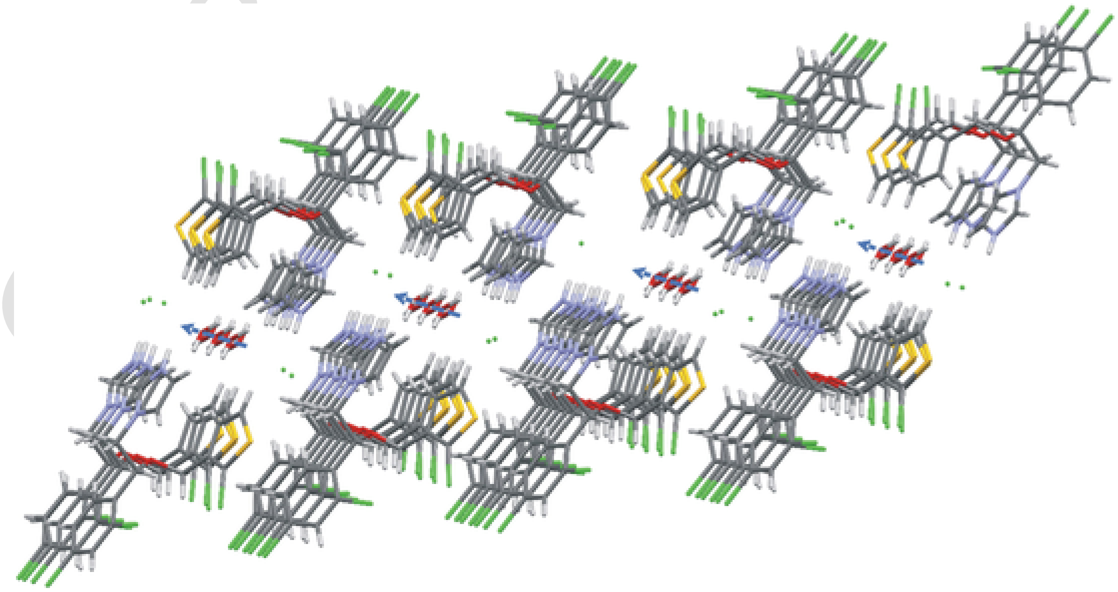

Fig. 7. Crystal structure of TCZHCl•½H_2O. Dashed arrows have been added as visual aids to highlight the location of the water channels.

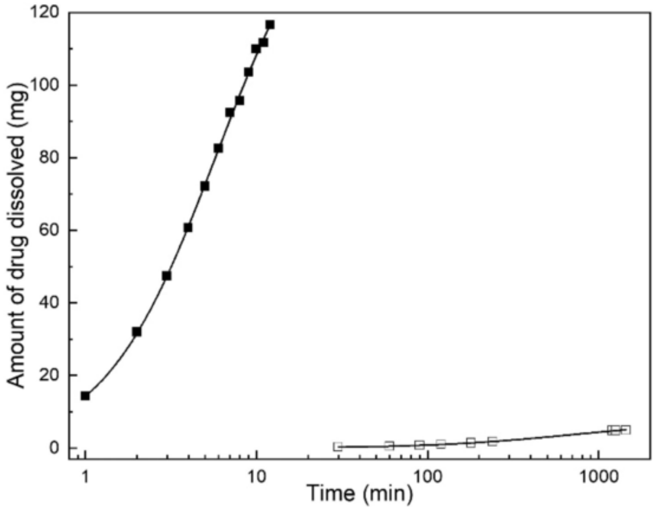

Fig. 8. Intrinsic dissolution rate test. Linear-log plot of the amount of drug dissolved in the dissolution medium as a function of time, for TCZHCl•½H_2O (■) and TCZ (□). Standard deviations marks (~1–2%) were omitted for the sake of clarity.

Contrastingly, however, the IDR of TCZHCl•½H_2O was determined as 1.81×10^{-1} mg cm^{-2} s^{-1} ($r^2 = 0.9953$, $n = 5$), representing a substantial increase of over 2000 times.

3.2.9.2. Dissolution of powders. The powder dissolution test was carried out at pH 4.5 (0.266 M acetate buffer) and in distilled water. It was observed (Fig. 9) that the dissolution rates depended on the nature of the solid, as well as on the pH of the medium used, in case of TCZ. It was verified that the behavior of the salt was essentially the same in both media, whereas it was noticed that the dissolution rate of pure TCZ was very slow in pure water (<6% after 24 h), exhibiting a notorious increase at pH 4.5, where it reached a level of 84% after 180 min. Contrastingly, however, 92% of the mass of the salt went into solution in the same medium, after only 1.5 min. The pH of the dissolution media remained essentially constant during the experiments. In the case of water, the initial pH of 6.96 dropped to 6.95 after dissolving TCZ for 1440 min and to 6.44 after completing the dissolution of TCZHCl•½H_2O.

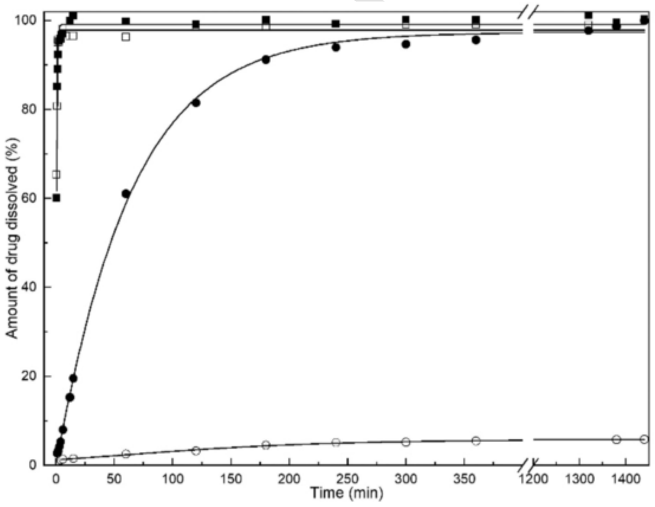

Fig. 9. Dissolution of powders containing TCZHCl•½H_2O (squares) and TCZ (circles) in 0.266 M acetate buffer pH 4.5 (filled) and in distilled water (empty).

Taken together, these improved properties of TCZHCl•½H_2O confirm its potential, which can derive into useful applications in the pharmaceutical field, such as new, more efficient formulations.

4. Conclusions

Tioconazole is a widely used antifungal agent and a scarcely soluble compound, with poor *in-vitro* dissolution characteristics; solid form manipulation has been only occasionally explored in the context of this active pharmaceutical ingredient. Salt formation is a convenient and attractive classical alternative to enhance drug dissolution and improve its pharmacological performance.

The hydrochloride hemihydrate salt of tioconazole (TCZHCl•½H_2O) was obtained and thoroughly characterized by vibrational (NIR, ATR/FT-IR) and NMR (^1H, ^{13}C and ^{15}N in DMSO-d_6 solution and ^{13}C and ^{15}N in the solid state) spectroscopies, as well as by PXRD and thermal methods (DSC, TGA).

Crystallization from aqueous hydrochloric acid produced crystals suitable for SC-XRD measurements, enabling solution and refinement of its crystal structure. The latter revealed that in the solid state tioconazole is protonated at the distal nitrogen atom of the imidazole ring, as verified by ^1H and ^{13}C NMR analysis. Additionally, comparison between the ^{13}C NMR data of TCZ and the salt suggested that the imidazole ring, which also undergoes conformational changes, participates in the delocalization of the positive charge resulting from protonation. Regarding the IDR results, TCZHCl•½H2O presented a dissolution rate three orders of magnitude higher than TCZ, evidencing the potential of the new hemihydrate. Analogous differences were observed during the dissolution of powders.

Summing up, this comprehensive study of TCZHCl•½H_2O provided valuable information about this solid, which may be useful at the time of designing new formulations based on this drug.

CRediT authorship contribution statement

Aldana B. Moroni : Methodology, Validation, Formal analysis, Investigation, Data curation, Writing – original draft, Writing – review & editing. **Elena Pérez Mayoral :** Conceptualization, Validation, Formal analysis, Resources, Writing – review & editing, Supervision. **Diego F. Lionello :** Methodology, Validation, Formal analysis, Data curation, Writing – review & editing. **Daniel R. Vega :** Conceptualization, Validation, Formal analysis, Resources, Writing – review & editing, Supervision. **Teodoro S. Kaufman :** Conceptualization, Validation, Formal analysis, Resources, Writing – original draft, Writing – review & editing, Visualization, Supervision, Project administration, Funding acquisition. **Natalia L. Calvo :** Conceptualization, Methodology, Validation, Formal analysis, Investigation, Data curation, Writing – original draft, Writing – review & editing, Visualization, Supervision.

Declaration of Competing Interest

The authors declare that they have no known competing financial interests or personal relationships that could have appeared to influence the work reported in this paper.

Data availability

Data will be made available on request.

Acknowledgements

The authors gratefully acknowledge Consejo Nacional de Investigaciones Científicas y Técnicas (CONICET, PUE IQUIR 2016, PIP 2021-0765), Agencia Nacional de Promoción Científica y Tecnológica (ANPCyT, PICT 2019-1155), Agencia Santafesina de Ciencia, Tecnología e Innovación (ASaCTeI, Project IO2019-302, BMG-N-2021-134) for financial support. The enthusiastic support and capable assistance of Dr. María Ángeles García Fernández (NMR Service, UNEDLAB, UNED) are gratefully acknowledged. ABM is also thankful to CONICET for her Doctoral fellowship, and Fundación Carolina is acknowledged for supporting a short stay of NLC at the UNED (Madrid, Spain). BSc. Cynthia Hucailuk and Cristian Oubiña are acknowledged for technical assistance with PXRD, TGA and DSC determinations.

Appendix A. Supplementary data

Supplementary data to this article can be found online at https://doi.org/10.1016/j.ijpharm.2023.122869.

References

Bharate, S., 2021. Recent developments in pharmaceutical salts: FDA approvals from 2015 to 2019. Drug Discov. Today 26, 384–398. https://doi.org/10.1016/j.drudis.2020.11.016.

Blokhina, S., Ol'khovich, M., Sharapova, A., Perlovich, G., 2021. Sublimation thermodynamics of antifungal drugs: Tioconazole, miconazole and climbazole. Fluid Phase Equilib. 544–545, 113098. DOI: 10.1016/j.fluid.2021.113098.

Brown, E.D., El Zahed, S.S., Farha, M.A., French, S., Kumar, G., 2021. Physicochemical and structural parameters contributing to the antibacterial activity and efflux susceptibility of small-molecule inhibitors of Escherichia coli. Antimicrob. Agents Chemother. 65, E01925–E02020. https://doi.org/10.1128/AAC.01925-20.

Budagumpi, S., Haque, R.A., Salman, A.W., Ghdhayeb, M.Z., 2012. Mercury (II)-and silver (I)-N-heterocyclic carbene complexes of CNC pincer-type ligands: Synthesis, crystal structures and Hofmann-type elimination studies. Inorg. Chim. Acta 392, 61–72. https://doi.org/10.1016/j.ica.2012.06.044.

Bunaciu, A.A., Udriştioiu, E.G., Aboul-Enein, H.Y., 2015. X-Ray Diffraction: instrumentation and applications. Crit. Rev. Anal. Chem. 45, 289–299. https://doi.org/10.1080/10408347.2014.949616.

Calvo, N.L., Alvarez, V.A., Lamas, M.C., Leonardi, D., 2019a. New approaches to identification and characterization of tioconazole in raw material and in pharmaceutical dosage form. J. Pharm. Anal. 9, 40–48. https://doi.org/10.1016/j.jpha.2018.11.006.

Calvo, N.L., Sreekumar, S., Svetaz, L.A., Lamas, M.C., Moerschbacher, B.M., Leonardi, D., 2019b. Design and characterization of chitosan nanoformulations for the delivery of antifungal agents. Int. J. Mol. Sci. 20, 3686. https://doi.org/10.3390/ijms20153686.

Calvo, N.L., Svetaz, L.A., Alvarez, V.A., Quiroga, A.D., Lamas, M.C., Leonardi, D., 2019c. Chitosan-hydroxypropyl methylcellulose tioconazole films: A promising alternative dosage form for the treatment of vaginal candidiasis. Int. J. Pharm. 556, 181–191. https://doi.org/10.1016/j.ijpharm.2018.12.011.

Chavan, R.B., Bhargavi, N., Lodagekar, A., Shastri, N.R., 2017. Near infrared spectroscopy: a tool for solid state characterization. Drug Discov. Today 22, 1835–1843. https://doi.org/10.1016/j.drudis.2017.09.002.

Crisóstomo-Lucas, C., García-Holley, P., Hernández-Ortega, S., Sánchez-Bartéz, F., Gracía-Mora, I., Barba-Behrens, N., 2015. Structural characterization and cytotoxic activity of tioconazole coordination compounds with cobalt(II), copper(II), zinc(II) and cadmium(II). Inorg. Chim. Acta 438, 245–254. https://doi.org/10.1016/j.ica.2012.11.026.

Drozd, K.V., Manin, A.N., Boycov, D.E., Churakov, A.V., Perlovich, G.L., 2021. Pharmaceutical multicomponent crystals of antifungal drugs with improved dissolution performance. Cryst. Growth Des. 21, 7285–7297. https://doi.org/10.1021/acs.cgd.1c01139.

Etherson, K., Dunn, C., Matthews, W., Pamelund, H., Barragat, C., Sanderson, N., Izumi, T., da Costa Mathewse, C., Halbert, G., Wilson, C., McAllister, M., Mann, J., Østergaard, J., Butler, J., Khadra, I., 2020. An interlaboratory investigation of intrinsic dissolution rate determination using surface dissolution. Eur. J. Pharm. Biopharm. 150, 24–32. https://doi.org/10.1016/j.ejpb.2020.02.005.

Farrugia, L.J., 2012. WinGX and ORTEP for Windows: An update. J. Appl. Cryst. 45, 849–854. https://doi.org/10.1107/S0021889812029111.

Flores, F.C., Paese, K., Weber, J., Antunes, J.B., Pohlmann, A.R., Guterres, S.S., Beck, R.C.R., Da Silva, C.D.B., 2017a. Lipid nanoparticles obtained with innovative natural materials for topical delivery of tioconazole: Mangospheres. J. Nanosci. Nanotechnol. 17, 1762–1770. https://doi.org/10.1166/jnn.2017.13019.

Flores, F.C., Rosso, R.S., Cruz, L., Beck, R.C.R., Silva, C.B., 2017b. An innovative polysaccharide nanobased nail formulation for improvement of onychomycosis treatment. Eur. J. Pharm. Sci. 100, 56–63. https://doi.org/10.1016/j.ejps.2016.12.043.

Fung, B.M., Khitrin, A.K., Ermolaev, K., 2000. An improved broadband decoupling sequence for liquid crystals and solids. J. Magn. Reson. 142, 97–101. https://doi.org/10.1006/jmre.1999.1896.

Gymer, G.E., 1977. 1-aryl-2-(1-imidazolyl) alkyl ethers and thioethers. Patent US4062966.

Hossain Mithu, M.S., Economidou, S., Trivedi, V., Bhatt, S., Douroumis, D., 2021. Advanced methodologies for pharmaceutical salt synthesis. Cryst. Growth Des. 21, 1358–1374. https://doi.org/10.1021/acs.cgd.0c01427.

Joshi, B.D., Mishra, R., Tandon, P., Oliveira, A.C., Ayala, A.P., 2014. Quantum chemical studies of structural, vibrational, NBO and hyperpolarizability of ondansetron hydrochloride. J. Mol. Struct. 1058, 31–40. https://doi.org/10.1016/j.molstruc.2013.10.062.

Kaplan, S.A., 1972. Biopharmaceutical considerations in drug formulation design and evaluation, Drug Metab. Rev. 1, 15–34. https://doi.org/10.3109/03602537208993907.

Kiss, E., Szabó, V.A., Horváth, P., 2019. Simple circular dichroism method for selection of the optimal cyclodextrin for drug complexation. J. Incl. Phenom. Macrocycl. Chem. 95, 223–233. https://doi.org/10.1007/s10847-019-00938-2.

Kljun, J., Scott, A.J., Lanisnik Rizner, T., Keiser, J., Turel, I., 2014. Synthesis and biological evaluation of organoruthenium complexes with azole antifungal agents. first crystal structure of a tioconazole metal complex. Organometallics 33, 1594–1601. https://doi.org/10.1021/om401096y.

Koral, E., Oswald, M., 1999. Multi-phase compositions for an initial and delayed release of a vaginal medicament. Patent US5985319.

Krause, L., Herbst-Irmer, R., Sheldrick, G.M., Stalke, D., 2015. Comparison of silver and molybdenum microfocus X-ray sources for single-crystal structure determination. J. Appl. Crystallogr. 48, 3–10. https://doi.org/10.1107/S1600576714022985.

Panini, P., Boel, E., Van Meervelt, L., Van den Mooter, G., 2022. Solvatomorphism in miconazole: the role of weak C–H···Cl hydrogen bonds and C–Cl···Cl–C halogen interactions in similarities and differences in the crystal packing. Cryst. Growth Des. 22, 2703–2724. https://doi.org/10.1021/acs.cgd.2c00112.

Penn, S.G., Goodall, D.M., Loran, J.S., 1993. Differential binding of tioconazole enantiomers to hydroxypropyl-β-cyclodextrin studied by capillary electrophoresis. J. Chromatogr. 636, 149–152. https://doi.org/10.1016/0021-9673(93)80067-i.

Penn, S.G., Bergstroem, E.T., Goodall, D.M., Loran, J.S., 1994. Capillary electrophoresis with chiral selectors: optimization of separation and determination of thermodynamic parameters for binding of tioconazole enantiomers to cyclodextrins. Anal. Chem. 66, 2866–2873. https://doi.org/10.1021/ac00090a012.

Pieńko, T., Grudzień, M., Taciak, P.P., Mazurek, A.P., 2017. Adsorption of antifungal drugs inside pristine and functionalized fullerenes and nanotubes: DFT investigation. Curr. Comp.-Aided Drug Des. 13, 177–185. https://doi.org/10.2174/1573409913666170303112858.

Ribeiro, R.F., Motta, M.H., Härter, A.P.G., Flores, F.C., Beck, R.C.R., Schaffazick, S.R., De Bona Da Silva, C., 2016. Spray-dried powders improve the controlled release of antifungal tioconazole-loaded polymeric nanocapsules compared to with lyophilized products. Mater. Sci. Eng. C 59, 875–884. https://doi.org/10.1016/j.msec.2015.10.035.

Sah, S.K., Badola, A., Mukhopadhyay, S., 2017. Development and evaluation of tioconazole loaded emulgel. Int. J. Appl. Pharm. 9, 83–90. https://doi.org/10.22159/ijap.2017v9i5.20046.

Sanli, S., Basaran, F., Sanli, N., Akmese, B., Bulduk, I., 2013. Determination of dissociation constants of some antifungal drugs by two different methods at 298 K. J. Sol. Chem. 42, 1976–1987. https://doi.org/10.1007/s10953-013-0083-x.

Sheldrick, G.M., 2008. A short history of SHELX. Acta Cryst. A64, 112–122. https://doi.org/10.1107/S0108767307043930.

Sheldrick, G.M., 2015. Crystal structure refinement with SHELXL. Acta Cryst. C71, 3–8. https://doi.org/10.1107/S2053229614024218.

Spek, A.L., 2009. Structure validation in chemical crystallography. Acta Cryst. D 65, 148–155. https://doi.org/10.1107/S090744490804362X.

Stratton, C.F., Newman, D.J., Tan, D.S., 2015. Cheminformatic comparison of approved drugs from natural product versus synthetic origins. Bioorg. Med. Chem. Lett. 25, 4802–4807. https://doi.org/10.1016/j.bmcl.2015.07.014.

Subashchandrabose, S., Saleem, H., Erdogdu, Y., Dereli, O., Thanikachalam, V., Jayabharathi, J., 2021. Structural, vibrational and hyperpolarizability calculation of (E)-2-(2-hydroxybenzylideneamino)-3-methylbutanoic acid, Spectrochim. Acta A 86, 231–241. https://doi.org/10.1016/j.molstruc.2013.10.062.

Van Doorne, H., Bosch, E.H., Lerk, C.F., 1988. Formation and antimicrobial activity of complexes of β-cyclodextrin and some antimycotic imidazole derivatives. Pharm. Weekbl. (Sci.) 10, 82–85. https://doi.org/10.1007/BF01962683.

Vioglio, P.C., Chierotti, M.R., Gobetto, R., 2017. Pharmaceutical aspects of salt and cocrystal forms of APIs and characterization challenges. Adv. Drug Deliv. Rev. 117, 86–110. https://doi.org/10.1016/j.addr.2017.07.001.

Yang, W., Wiederhold, N.P., Williams, III, R.O., 2008. Drug delivery strategies for improved azole antifungal action. Expert Opin. Drug Deliv. 5, 1199–1216. https://doi.org/10.1517/17425240802457188.

Zakeri-Milani, P., Barzegar-Jalali, M., Azimi, M., Valizadeh, H., 2009. Biopharmaceutical classification of drugs using intrinsic dissolution rate (IDR) and rat intestinal permeability. Eur. J. Pharm. Biopharm. 73, 102–106. https://doi.org/10.1016/j.ejpb.2009.04.015.